JGR

RESEARCH ARTICLE

Key Points:
- Highest tropical convection controls tropical tropopause CO
- Tropical tropopause heating rate distribution affects tracer distribution
- Tibetan Plateau convection is important for Asian anticyclone CO concentration

Correspondence to:
E. J. Jensen,
eric.j.jensen@nasa.gov

Investigation of the transport processes controlling the geographic distribution of carbon monoxide at the tropical tropopause

E. J. Jensen[1], L. Pfister[1], R. Ueyama[1], J. W. Bergman[2,3], and D. Kinnison[3]

[1]NASA Ames Research Center, Moffett Field, California, USA, [2]Bay Area Environmental Research Institute, Sonoma, California, USA, [3]National Center for Atmospheric Research, Boulder, Colorado, USA

Abstract Convectively influenced trajectory calculations are used to investigate the impact of different Tropical Tropopause Layer (TTL) transport pathways for establishing the distribution of carbon monoxide (CO) at 100 hPa as observed by the Microwave Limb Sounder (MLS) on board the Aura satellite. Carbon monoxide is a useful tracer for investigating TTL transport and convective influence because the CO lifetime ($\simeq$1–2 months) is comparable to the time required for slow ascent through the TTL. MERRA horizontal winds are used for the diabatic trajectories, and off-line calculations of TTL radiative heating are used to determine the vertical motion field. The locations and times of convective influence events along the trajectories are determined from 3-hourly, geostationary satellite measurements of convective clouds. The trajectory model reproduces most of the prominent features in the 100 hPa CO geographic distribution indicated by the MLS observations for the winter and summer 2007 periods simulated. CO concentrations and tendencies simulated with the Whole Atmosphere Climate Chemistry Model (WACCM) are used to specify boundary-layer concentrations for convective influence and CO loss rates resulting from reaction with OH. The broad maximum in CO concentration over the Pacific during Boreal winter is primarily a result of the strong radiative heating (corresponding to upward vertical motion) associated with the abundant TTL cirrus in this region. Convection over the Pacific brings clean maritime air to the tropopause region and actually decreases the 100 hPa CO. The relative abundance of CO over the continental convective regions during wintertime is sensitive to small variations in convective cloud-top height. Both the simulated and the observed summertime 100 hPa CO distributions are dominated by the maximum co-located with the upper level anticyclone forced by the Asian monsoon convection. Sensitivity tests indicate that the summertime Asian monsoon anticyclone 100 hPa CO maximum is dominated by extreme convective systems with detrainment of polluted air above about 360–365 K potential temperature. This result stems directly from the fact that the heating rates are negative (downward motion) below 360–365 K during summertime through most of the tropics; therefore, air detrained from convection at lower levels will generally just sink back down into the middle troposphere. We find that most of the CO feeding into the Asian monsoon anticyclone comes from convection over the Tibetan Plateau and India, with relatively minor contributions from southeast Asia and eastern China.

1. Introduction

The great majority of the irreversible, troposphere-to-stratosphere transport occurs across the tropical tropopause [*Holton et al.*, 1995], and as such, the composition of the tropical tropopause region represents a lower boundary condition for the composition of the entire stratosphere. The atmospheric layer bracketing the tropical tropopause, which shares dynamical and chemical properties of both the troposphere and stratosphere, has been referred to as the Tropical Tropopause Layer (TTL) [*Fueglistaler et al.*, 2009]. The lower TTL boundary is typically defined as the main tropical convective outflow height ($\simeq$13 km), and the upper boundary is typically taken to be the highest altitude reached by extreme convective systems (19–20 km). TTL transport (and ultimately the composition of air entering the stratosphere) is controlled by a blend of large-scale advection and extreme deep convection penetrating well into the TTL, sometimes extending above the tropopause [*Adler and Mack*, 1986]. Above about 15 km, air is slowly ascending (as part of the Brewer-Dobson circulation [*Brewer*, 1949]), with radiative heating balancing this slow ascent. The time scale for large-scale transport from 15 to 19 km is on the order of 1–3 months [*Rosenlof*, 1995; *Mote et al.*, 1996; *Schoeberl et al.*, 2008]. In contrast, the time scale for transport from the boundary layer to the TTL in

convective updrafts can be less than an hour. The relative mass flux associated with these transport pathways will, in part, determine the stratospheric concentration of gases with losses and sources in the TTL, with the rapid convective path having particular importance for species with short lifetimes.

The influence of deep convection on TTL composition has proven difficult to evaluate, partly because of limitations in the global measurements of convective cloud-top height [*Liu et al.*, 2007]. In particular, there has been considerable debate about the importance of rare convective systems that overshoot their level of neutral buoyancy and detrain air near (or above) the tropical tropopause [*Randel and Jensen*, 2013]. Rapid TTL horizontal transport disperses the tracer anomalies caused by convective systems, making the effects of large-scale transport and convection difficult to distinguish. There are notable exceptions to this statement, particularly the TTL in Boreal summertime over eastern Asia where the monsoon convection provides a strong, consistent convective source of lower tropospheric trace gases to the TTL, and confinement in the associated anticyclone allows tracer perturbations to build up and persist [*Filipiak et al.*, 2005; *Li et al.*, 2005; *Fu et al.*, 2006; *Randel and Park*, 2006]. Evaluation of convective influence on TTL composition using global models is hindered by limitations of convective parameterizations. The height distribution of convective cloud tops in the tropical tropopause region depends on a number of small-scale processes, such as entrainment into convective updrafts, that cannot be directly represented by parameterizations using resolved state variables at current global (or even regional) model spatial resolutions.

The need for an improved understanding of TTL transport pathways is additionally motivated by the expectations for transport changes in a changing climate. Global model simulations consistently predict a strengthening of the Brewer-Dobson circulation [*Butchart*, 2014], with a corresponding decrease in the time required for large-scale transport through the TTL. Additionally, warmer sea-surface temperatures in a future climate present at least the potential for increased convective intensity [e.g., *Emanuel*, 1987; *Knutson et al.*, 2010].

In this study, we examine the transport processes that determine CO concentrations at the tropical tropopause, including convective transport. This species is used because (1) the budget of CO has been extensively studied and is relatively well understood and (2) carbon monoxide has been extensively observed through the depth of the troposphere and stratosphere. In particular, the Aura Microwave Limb Sounder provides global measurements of CO with adequate spatial and temporal sampling frequencies to permit examination of regional tracer distributions and their variations on weekly time scales. The dominant sink of CO is oxidation by the hydroxyl radical (OH), and its photochemical chemical lifetime is on the order of 1–3 months [*Xiao et al.*, 2007]. Since this lifetime is comparable to the time required for slow ascent through the TTL, there is a strong vertical gradient in TTL CO concentration, and rapid transport by deep convection has distinct impacts on the regional distribution of CO. There is also a strong seasonal cycle in tropopause-level CO associated with seasonal variations in deep convection, pollution sources, and TTL upwelling [*Schoeberl et al.*, 2006; *Wang et al.*, 2014]. We will specifically focus on Boreal wintertime (early February) when the 100 hPa CO has a broad maximum over the Pacific and central America and summertime (late August) when the Asian monsoon and its associated upper tropospheric anticyclone dominate the CO regional variability.

Wang et al. [2014] recently used forward, domain-filling trajectories to simulate stratospheric CO concentration. Seasonal and interannual variations in the distribution of these tracers were shown to be strongly sensitive to changes in the tropical upwelling. The approach used here is similar in that we are using trajectories initialized with MLS measurements to simulate CO. The primary differences are (1) we are focusing on the regional distribution of tracers within the TTL and (2) we use satellite measurements of cloud top heights to diagnose convective influence on TTL tracers, whereas convective influence is not explicitly included in the *Wang et al.* [2014] study.

Transport through the TTL has been modeled with a variety of approaches, including global Eulerian models driven by meteorological analysis winds [e.g., *Bannister et al.*, 2004; *Park et al.*, 2009], kinematic back trajectories [e.g., *Gettelman et al.*, 2002; *Fueglistaler et al.*, 2004; *Bergman et al.*, 2013], and forward domain-filling trajectories [e.g., *Schoeberl and Dessler*, 2011; *Wang et al.*, 2014]. Each of these approaches has advantages and disadvantages. In global Eulerian models, convective transport is represented by parameterizations that both redistribute the tracers directly via mixing through the depth of the diagnosed convection and indirectly via the convective latent heating that drives upward motion on the resolved grid scale. In the kinematic trajectory approach, convective transport is also represented by the resolved winds,
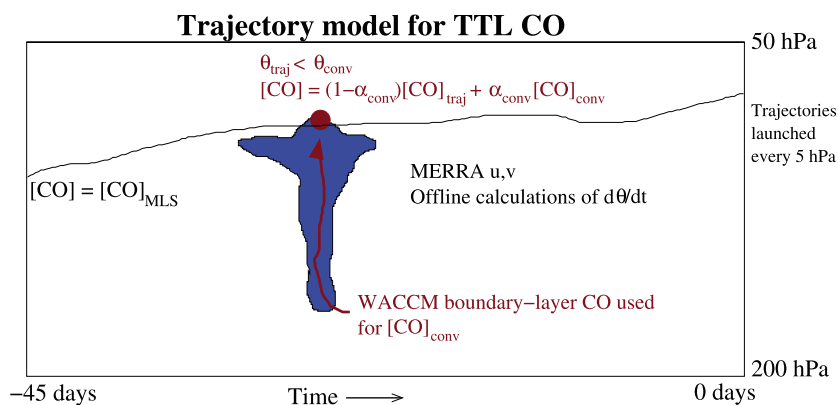
Figure 1. The approach used for convectively influenced calculations of CO concentrations along trajectories is shown schematically. Forty-five day back trajectories are run from a grid of latitudes and longitudes throughout the tropics, at a range of pressure levels, and every 6 h over 1 week time periods. CO concentrations are initialized (at the earliest time) using MLS data. MERRA horizontal winds and offline radiative transfer calculations [*Yang et al.*, 2010] of $d\theta/dt$ are used for the diabatic trajectory calculations. At intersections with deep convection (red circle), the CO concentration is adjusted based on the WACCM boundary-layer CO concentration and an assumed degree of entrainment at cloud-top (α_{conv}). The final profiles of CO (latest times) are convolved with the appropriate a prioris and averaging kernels for comparison with MLS CO retrievals.

which ultimately depend on the convective parameterizations. As discussed above, the convective parameterizations do not necessarily properly represent the vertical distribution of deep convection extending into the TTL. In addition, kinematic trajectories suffer from vertical velocity "noise" that can result in artificial vertical diffusion [*Schoeberl and Dessler*, 2011]. With diabatic trajectory calculations, the vertical motion is determined from radiative-transfer calculations of the net heating rate. The convectively influenced, diabatic trajectory approach used here relies on satellite measurements of convective clouds at the times and locations of the trajectories to determine when and where convective influence occurs. Within the limits of satellite cloud-top height measurements, this approach should reasonably represent the height distribution of convective influence.

We begin by describing the methodology and evaluating the modeling approach by comparing the calculated CO distribution at 100 hPa with MLS observations. Next, we use sensitivity studies to evaluate the impact of varying convective cloud top height and the distribution of TTL radiative heating (vertical ascent). Lastly, we assess the robustness of the results by testing the sensitivity of the 100 hPa CO distribution to various model assumptions and forcing fields.

2. Convectively Influenced Trajectory Approach

We use a convectively influenced trajectory model including CO loss due to reaction with OH to calculate the time evolution of CO concentration in parcels transiting through the TTL. The oxidation loss rates are taken from global chemistry model simulations, as described below. Convective influence is diagnosed by tracing the trajectories through geostationary satellite measurements of cloud tops. The approach for identifying convective cloud top locations and heights in the satellite data is described in detail below. The elements of the model for calculating CO concentrations are shown schematically in Figure 1.

Horizontal winds from the NASA Modern Era Retrospective-Analysis for Research and Applications (MERRA) analyses are used for the trajectory calculations. We use the diabatic trajectory approach, in which vertical velocity (with potential temperature as the vertical coordinate) is calculated from the diabatic heating rates. Above about 150 hPa, the diabatic heating is dominated by radiative heating, and other terms in the thermodynamic equation (such as latent heating) are negligible [*Wright and Fueglistaler*, 2013]. The TTL diabatic heating fields in meteorological analyses differ substantially from one model to another [*Wright and Fueglistaler*, 2013; *Randel and Jensen*, 2013], primarily because of the large impact of clouds (and their redistribution of water vapor) and the disparity between cloud representations in the different models. Note the strong sensitivity of TTL radiative heating rates to clouds below the TTL, which affect the upwelling longwave radiation in the TTL, as well as clouds within the TTL, which locally enhance radiative

heating. Here, we use off-line calculations of TTL radiative heating based on satellite measurements of cloud distributions [*Yang et al.*, 2010]. Although the off-line calculations are uncertain because of limitations in the cloud measurements, the heating rates in the analysis models are likely to be less representative of reality given the challenge of simulating clouds in global models. The MERRA TTL heating rates are quite different from those calculated by *Yang et al.* [2010] using cloud observations [*Randel and Jensen*, 2013], partly because of considerable smoothing of the heating rates in MERRA. Also, it has been shown that the ECMWF ERA-interim heating rates are significantly higher, resulting in short residence times in the TTL [*Wang et al.*, 2014]. Given these discrepancies and the known problems with cloud fields in global models that ultimately result in heating rate errors, we have not included sensitivity tests using the MERRA radiative heating rates.

We focus here on 100 hPa concentrations in the tropics for a number of reasons. At this vertical level, considerable influence of convection should be apparent, both from extreme systems that reach 100 hPa and from convection affecting parcels at lower levels that subsequently ascend to 100 hPa. As discussed below, the MLS CO product has relatively coarse vertical resolution, and the data product at 100 hPa is preferable over the 68 and 146 hPa data products for evaluating competition between slow ascent through the TTL and convective influence. Also, 100 hPa is the MLS level nearest the tropical tropopause, and, as discussed above, there is currently interest in understanding processes controlling the composition at the lower boundary of the stratosphere.

We run sets of back trajectories from locations every 2° latitude and longitude, and from pressure levels every 5 hPa ranging from 50 to 200 hPa. Sets of trajectories are launched every 6 h for 1 week periods in 2007 during Boreal winter (early February) and Boreal summer (late August). The CO concentration is initialized at the end of the back trajectories (earliest time) by interpolating to the nearest MLS vertical profile. We find that the calculated CO at the latest trajectory time is insensitive to the geographic distribution of CO determined from MLS for initialization because most of the parcels have their CO concentration modified by convective encounters. The CO concentration is then integrated forward in time along the trajectories using loss rates extracted from Whole Atmosphere Climate Chemistry Model (WACCM) simulations. (See discussion of WACCM CO simulations below.) When our convective influence analysis indicates that the parcels intersected anvil clouds, the CO concentration is adjusted using the WACCM boundary-layer CO concentration at the corresponding latitude, longitude, and time.

The concentration of tracers detrained from the tops of deep convection is necessarily some mixture of boundary-layer tracer concentration, and the concentration of air entrained into the convective system through the full depth of the cloud system. Quantification of entrainment rates into deep convection has proven challenging, and the degree of entrainment doubt varies widely from one convective system to another. The boundary-layer concentration used here is calculated including WACCM model levels with pressures greater than 85% of the surface pressure (approximately 1.5 km above the surface); the results are not strongly sensitive to the choice of the boundary layer top pressure. This approach undoubtedly overemphasizes the low-level CO field. We also use sensitivity tests to evaluate the impact of specifying the convective detrainment CO concentrating as the average of WACCM values from the surface to the top of the convective clouds.

Entrainment is also known to be particularly strong near the turbulent tops of the deep convective systems. Therefore, the CO concentration in the convective outflow plumes presumably represents a mixture of the detrained concentration and the local concentration before the convective intrusion. We evaluate the impact of this entrainment using sensitivity tests with a fractional convective influence α_{conv} such that the concentration at the convective encounter is set to

$$[CO] = (1 - \alpha_{\mathrm{conv}})[CO]_{\mathrm{traj}} + \alpha_{\mathrm{conv}}[CO]_{\mathrm{conv}} \qquad (1)$$

where $[CO]_{\mathrm{traj}}$ and $[CO]_{\mathrm{conv}}$ are the trajectory calculation of CO up to the convective encounter time and the WACCM boundary-layer CO at the location of the convection, respectively.

The trajectory length (45 days) is chosen such that most of the trajectories experienced convective influence. Using shorter trajectories would not serve our purpose because the final tracer distribution would primarily represent transport of the values initialized from MLS, without a complete picture of convective influence. Sensitivity tests discussed below show that increasing the length of the trajectories does not significantly change the calculated 100 hPa CO distributions.
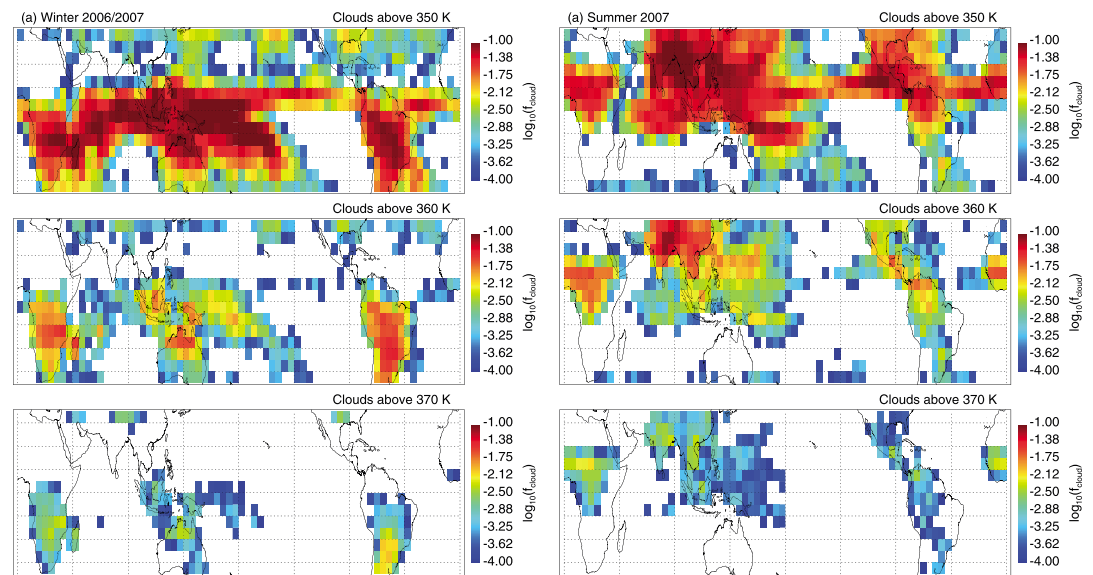
Figure 2. The frequency of occurrence for convective clouds extending above different potential temperature levels (top: 350 K; middle: 360 K; bottom: 370 K). (left column) Winter 2006/2007. (right column) Summer 2007. Note the use of a logarithmic cloud frequency scale to cover the wide dynamic range.

2.1. Convective Influence Calculations

Our approach involves diagnosing the influence of convection on tracer concentrations along trajectories. Specifically, we account for the modification of CO concentration along the trajectories as a result of air detrained from deep convection that carries CO abundances from the lower troposphere. Essentially, we trace the time/longitude/latitude paths of the trajectories through time varying longitude/latitude fields of convective cloud top potential temperature, identifying locations where the cloud top potential temperature exceeds the parcel potential temperature. We assume that parcel tracer concentration will be affected by the convection even if the parcel is well below the cloud top.

The time scale of deep tropical convective systems is measured in hours rather than days, so a high-frequency, global measure of deep convective input is desirable. The best way to obtain this cloud-top field is by relating geostationary infrared (IR) brightness temperatures to meteorological analysis temperatures, taking advantage of decreasing temperatures with altitude. To separate actual convective systems from synoptic cloud systems, we use a rainfall threshold, applied based on the 3-hourly global combined IR/microwave precipitation estimates at quarter degree resolution [*Huffman et al.*, 2007]. Effective brightness temperatures for quarter degree regions meeting the rainfall threshold are set to a value 2 standard deviations lower than the mean of all the 4 km pixels for that quarter degree region (reflecting the fact that anvils are flat rather than umbrella shaped).

To convert brightness temperature to a cloud top potential temperature, we assume that the deep convective cloud perturbs the analysis temperature profile by mixing with the environment above some appropriate potential temperature level of neutral buoyancy, which we take to be 355 K for oceanic areas and 365 K for continental areas. A mixed temperature profile (70% convective plume following a moist adiabat and 30% environment) is generated, and the effective brightness temperature from the geostationary satellite imagery is matched to this mixed temperature profile. Previous work [*Sherwood et al.*, 2004; *Minnis et al.*, 2008] has shown that IR methods tend to underestimate cloud altitude (due to the fact that the radiation detected by the IR sensor originates some distance into the cloud) by about 1 km; thus, 1 km is added to the cloud altitude. The tunable parameters (e.g., the rainfall threshold, the 70–30 mixing ratio, and the 1 km enhancement) are arrived at by comparing the resulting convective cloud top distribution to convective cloud tops based on the CLOUDSAT deep convective cloud classification product [*Wang and Sassen*, 2001]. Since CLOUDSAT does not capture the full height of the deep convective cloud because of insensitivity to small particles, we also include nearly simultaneous CALIPSO measurements in the analysis. The method and its validation are described in Pfister et al. (in preparation, 2014).
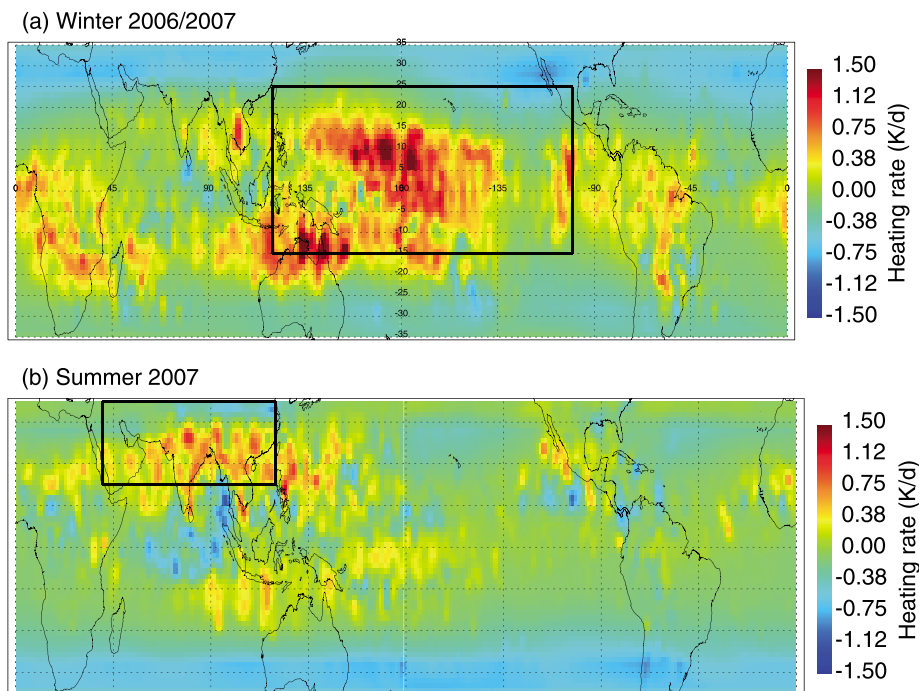
Figure 3. Net radiative heating rate at 365 K potential temperature for wintertime (19 December 2006 to 7 February 2007, top) and summertime (July–August 2007, bottom) based on offline radiative transfer calculations [*Yang et al.*, 2010]. The black boxes in the figures correspond to regions of enhanced 100 hPa CO. Average vertical profiles over these regions are shown in Figure 4.

The major effect of the mixing scheme (as opposed to simply matching the effective brightness temperature to the analysis temperature profile) is to lower the cloud top potential temperature. For most deep convective clouds in the tropics, which top out at 15 km or below, the effect is fairly small. For the coldest cloud tops, however, the mixing scheme lowers cloud tops by about 1 km or so (as compared to a simple temperature matching).
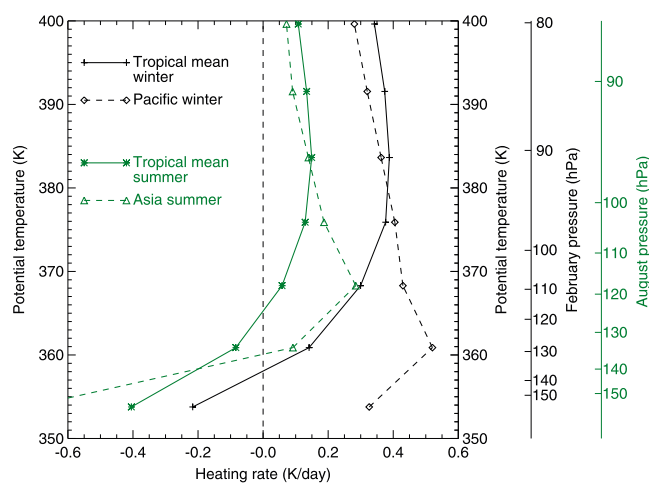

Figure 4. Net radiative heating rate vertical profiles from the *Yang et al.* [2010] calculations. Tropical mean winter and summer profiles are shown, as well as averages over the regions of high CO concentration indicated by the black boxes in Figure 3. Note the strong positive heating (upward motion) throughout the TTL over the wintertime Pacific. During summertime, upward motion will only occur above about 360–365 K potential temperature.

The geographic distributions of TTL convective clouds are shown in Figure 2. Note the use of a logarithmic scale for convective-cloud occurrence frequency to cover the wide dynamic range of values. The regions with convection routinely extending deep into the TTL are apparent: southern Africa, northern Australia, and the western Pacific during Boreal wintertime; and Asia, central Africa, and central America during summertime. The occurrence frequency of convective clouds that reach the upper TTL is strongly sensitive to the temperature-profile modifications for convection extending beyond the level of neutral buoyancy. The impact of these extreme convective clouds is discussed below.

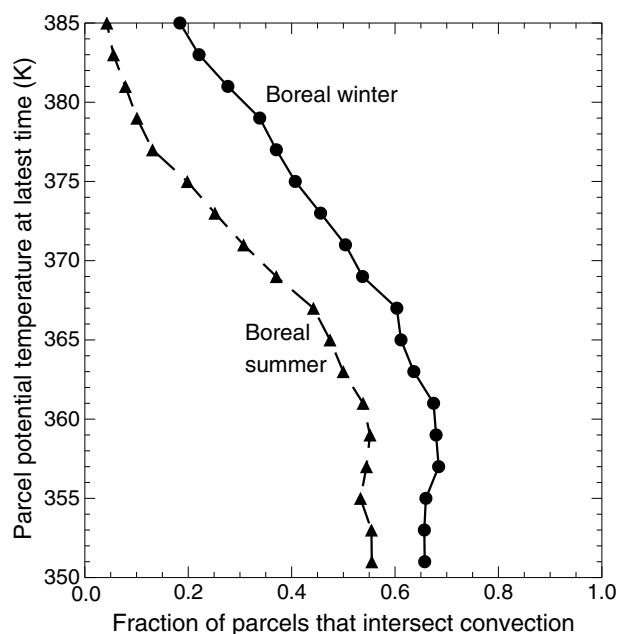As shown by *Bergman et al.* [2012], the most effective vertical transport

Figure 5. The fraction of parcels with convective influence is plotted versus their final (latest time) potential temperature. Solid curves with circles are calculations for trajectories ending 1–7 February 2007. Dashed curves with triangles are calculations for trajectories ending 25–31 August 2007.

of tropospheric air into the stratosphere occurs in regions with both relatively high deep convection and relatively strong radiative heating. The regional distributions of net radiative heating at ≃365 K potential temperature (from the *Yang et al.* [2010] calculations) for winter 2006/2007 and summer 2007 are shown in Figure 3. Figure 4 provides heating rate profiles, including both tropical mean profiles and profiles for selected regions indicated by the black boxes in Figure 3. The heating rate patterns primarily reflect the distributions of TTL temperature as well as tropical clouds at various altitudes. The wintertime western Pacific maximum reflects the cold tropopause temperatures and common occurrence of TTL cirrus there. During summertime, radiative heating is relatively strong over southern Asia, reflecting the Asian monsoon cloud effects. Weaker radiative heating (or cooling in some regions) generally prevails in the deep tropics during the summer as compared to winter. The vertical profiles of heating rate (Figure 4) indicate positive heating (upward motion) through most of the depth of the TTL during wintertime, with particularly strong, deep heating over the Pacific. During summertime, the zero radiative heating level is about 365 K potential temperature in the tropical mean and about 360 K over Asia. As discussed below, the fact that upward motion during summertime only occurs in the upper TTL over the Asian monsoon region means only the highest convective systems will influence the 100 hPa CO abundance. Note that 100 hPa corresponds to about 371 K potential temperature during Boreal wintertime and 378 K potential temperature during summertime.

The fractions of trajectories that are influenced by convection are plotted versus their final potential temperature in Figure 5. At potential temperatures below about 365–370 K, most parcels reach convection. Fewer parcels encounter convection along the summertime trajectories, primarily because the heating rates are weaker and most parcels from the mid-to-upper TTL do not make it down the lower TTL where convective clouds are commonplace. The majority of parcels ending above ≃370 K do not encounter convection along their 45 day journeys.

Figure 6 shows the vertical distribution of origin locations (at the earliest time along the trajectories) for parcels that ended up between 90 and 110 hPa (at the latest time along the trajectories). Separate curves are shown for parcels with or without convective origin. As expected, convective encounters typically occur in the lower TTL. The convective encounters occur at higher potential temperatures during summertime primarily because the vertical wind field (calculated from heating rates) does not take most parcels from 100 hPa down to the lowermost TTL [*Bergman et al.*, 2012]. Also, the potential temperature corresponding to a particular TTL pressure level (such as 100 hPa) is higher during the summer than during the winter (see Figure 4).

The geographic distribution of convective influence at 100 hPa is shown in Figure 7. The majority of wintertime parcels over a broad Pacific region reached convection (Figure 7, top). This Pacific maximum in convective influence results both from the frequent convection in the region and the broad, deep uplift over the Pacific (Figures 3 and 4). During summertime, convective influence at 100 hPa is limited to the region near the Asian monsoon and its associated anticyclone. This pattern is strongly influenced by the Asian monsoon anticyclone circulation in addition to the distribution of convection associated with the Asian
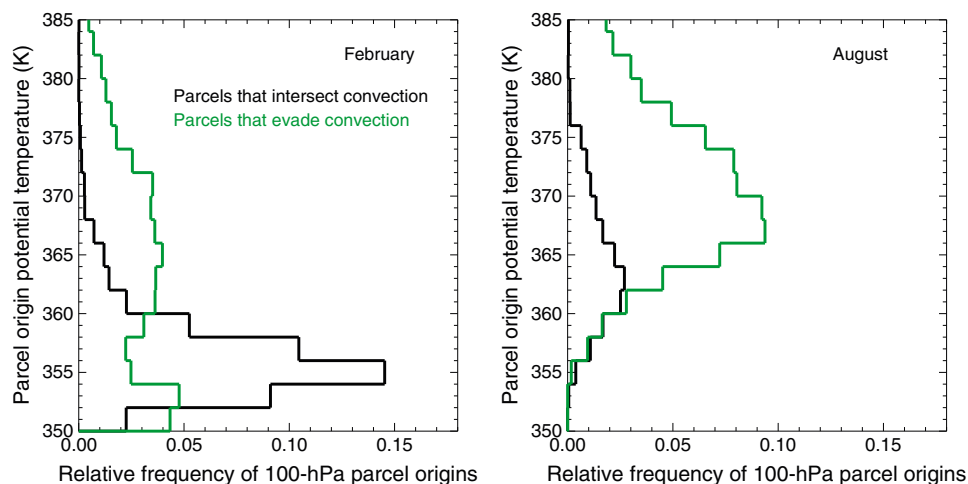
Figure 6. The frequency distributions of parcel initialization potential temperatures are plotted for parcels that ended (at the latest time) near 100 hPa. For parcels that intersected convection, the potential temperatures of the latest convective encounters are shown (black curves). Green curves are shown for parcels that did not reach convection. (left) Corresponds to trajectories ending 1–7 February 2007; (right) corresponds to trajectories ending 25–31 August 2007.

monsoon. The fractions of 100 hPa parcels with convective influence is lower in August primarily because of the weaker TTL radiative heating in the summertime than the wintertime.

3. MLS CO Measurements

Measurements of TTL CO from the Microwave Limb Sounder (MLS) on the Aura spacecraft are used both to initialize tracer concentrations at the earliest trajectory times and to evaluate our trajectory calculations
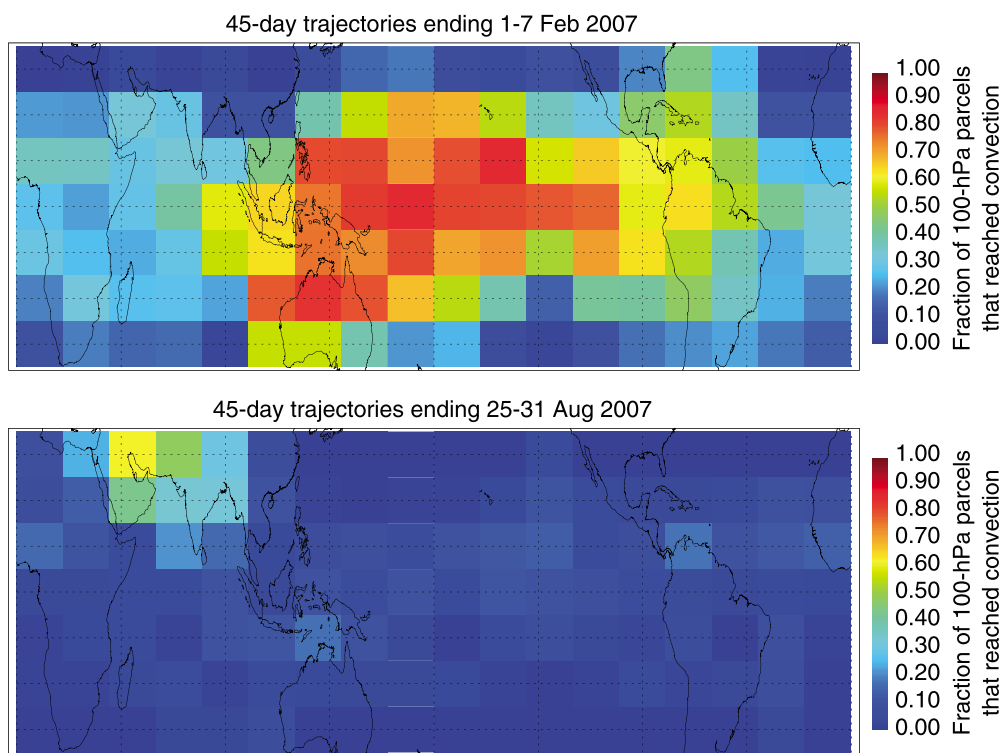

Figure 7. Maps of the fraction of back trajectories launched from near 100 hPa that reached convection. (top) Wintertime results are shown; (bottom) summertime results are shown. The regional distributions of both deep convection and TTL radiative heating contribute to the regional distribution of convective influence [*Bergman et al.*, 2012].

of CO. The MLS retrievals of CO, as well as the evaluation of MLS data products, are described in detail in a series of publications [e.g., *Livesey et al.*, 2008]. *Park et al.* [2013] showed that MLS 100 hPa CO concentrations are roughly 5–20 ppbv higher than corresponding retrievals from the Atmospheric Chemistry Experiment–Fourier Transform Spectrometer (ACE-FTS) solar occultation measurements, suggesting that the MLS CO concentrations may have a high bias at 100 hPa.

Given the sharp vertical gradients of TTL CO concentration and the fact that MLS retrievals of CO represent a vertical average over about 4.5 km, proper vertical averaging of the simulated CO concentrations over a range of pressure levels is essential for a meaningful comparison with MLS retrievals. As recommended in the MLS documentation, we first use linear, least-squares fitting to estimate model CO concentrations at the MLS pressure levels. Next we convolve the differences between the simulated concentrations and the MLS a priori with the MLS averaging kernels.

4. WACCM Simulations of Carbon Monoxide

The NCAR Whole Atmosphere Community Climate Model, version 4 (WACCM4), is a comprehensive numerical model spanning the range of altitude from the Earth's surface to the thermosphere [*Garcia et al.*, 2007; *Kinnison et al.*, 2007; *Marsh et al.*, 2013]. WACCM4 is based on the framework of the NCAR Community Atmosphere Model, version 4 (CAM4) and includes all of the physical parameterizations of CAM4 [*Neale et al.*, 2013], as well as a finite volume dynamical core [*Lin*, 2004] for the tracer advection. The chemical module includes a detailed representation of the chemical and physical processes in the troposphere through the lower thermosphere. The 168 species included in this mechanism are contained within the O_x, NO_x, HO_x, ClO_x, and BrO_x chemical families, along with CH_4 and its degradation products. In addition, 18 primary nonmethane hydrocarbons and related oxygenated organic compounds are represented along with their surface emissions [*Emmons et al.*, 2010; *Lamarque et al.*, 2012]. Recently, a new version of the WACCM model has been developed that allows the model to be run with specified (external) meteorological fields. This is achieved by relaxing the horizontal winds and temperatures to reanalysis fields and is referred to as Specified Dynamics (SD-WACCM). In this study, the WACCM4 meteorological fields are "nudged" with the SD meteorological fields using the approach described in *Kunz et al.* [2011]. Meteorological fields are taken from the NASA Global Modeling and Assimilation Office (GMAO) Modern-Era Retrospective Analysis for Research and Applications (MERRA) [*Reinecker et al.*, 2011]. The SD-WACCM version has been used in several UTLS studies of tracer transport in the upper troposphere/lower stratosphere region [e.g., *Randel et al.*, 2010; *Park et al.*, 2013]. Surface emissions of CO and NMHCs included in the model are specific to each year. Biomass burning emissions are monthly averages over 1997–2009 from the GFED-v2 inventory (see *van der Werf et al.* [2006] for details on inventory approach). Biofuel combustion emissions are constant year-round, which primarily consists of domestic heating and cooking.

Lamarque et al. [2012] compared model simulations of CO (using the same emissions database as in the WACCM run we are using here) with the Measurements of Pollution in The Troposphere (MOPITT) CO retrievals. A large, systematic high bias in the simulated CO over Africa is apparent [see *Lamarque et al.*, 2012, Figure 12], particularly during wintertime. This African CO high bias, presumably attributable to the emission database, is apparent as excessive convective CO at 100 hPa in our calculations, as discussed below.

The predominant sink for CO is oxidation by the hydroxyl radical (OH). Although specific numbers are often referred to for the CO lifetime, the OH concentration and corresponding rate of CO destruction are actually highly variable in space and time. As an example, the CO loss time at 100 hPa for the first week in February varies from less than 1 week to greater than 6 months. We evaluate the impact of this spatial variability by running sensitivity tests using zonal mean, altitude-dependent CO loss rates.

5. Uncertainties

The convectively influenced trajectory approach described above for simulating 100 hPa CO concentrations has a number of significant sources of uncertainty. The *Yang et al.* [2010] calculations of TTL radiative heating rate are dependent on imperfect satellite retrievals of cloud properties. In particular, the satellite-instrument retrievals of cloud properties generally provide little information about hydrometeor size, which affects the shortwave radiative transfer. Also, since the cloud measurements are sparse, considerable averaging is required to generate global fields. As a result, the heating rate fields are monthly means, and we are neglecting the considerable day-to-day (and even hour-to-hour) variability that must accompany the highly

variable cloud field. Neglecting high-frequency variations in heating rate may not affect the results a great deal since the effects of radiative heating (vertical motion) on the trajectories are only significant after integration over weeks. In other words, the large-scale vertical advection is slow, so high-frequency variability may average out to a large degree. *Bergman et al.* [2012] showed that high-frequency perturbations in the heating rate do not strongly affect the convective-origin statistics of parcels reaching 380 K potential temperature.

The CO concentration in an air parcel detrained from deep convection depends on the degree of entrainment into convective updrafts throughout the vertical column from the boundary layer to the cloud top. The efficiency of entrainment into convective updrafts is not well known and probably varies considerably from one type of convection to another (e.g., maritime versus continental). As discussed above, we attempt to bracket this uncertainty by using either boundary-layer CO concentrations (generally an upper limit) or below-cloud-top column average CO concentration (typically a lower value) for the detrained CO concentration. We also lack knowledge of the degree of entrainment of ambient air into convective plumes at the detrainment level. We bracket this problem by including a fractional convective influence on the CO concentration along the trajectories (α_{conv}) and varying this parameter between zero (no convective influence) and unity (no entrainment into convective plumes).

We are implicitly assuming that the horizontal extent of the convectively influenced plume of each cloud system is represented by the extent of the anvil cirrus detectable by infrared geostationary satellite measurements. This assumption creates an artificial dependence on ambient relative humidity where the detrainment occurs. In a humid environment, deep convection will generate a large, persistent anvil; whereas anvils produced by overshoots into dry air will be small and transient. Lastly, the convective systems no doubt modify the mesoscale flow field, producing divergence in the vicinity of the convective outflow. This divergence could effectively increase the radius of influence by drawing in trajectories (in reverse time) that approach the convective systems. Ultimately, the quantitative efficacy of our convective-influence approach must be verified by comparing the simulated CO fields to observations.

We argue that the approach employed here of using satellite measurements to determine the heights of convective cloud tops is preferable to relying on convective parameterizations in global models. However, there are significant uncertainties in the remote-sensing measurements of cloud-top height. As discussed above, we apply a 1 km offset to account for the low bias in infrared cloud-top height retrievals; however, the actual bias can be quite variable (ranging from about 0.5 to 2 km) [*Sherwood et al.*, 2004; *Minnis et al.*, 2008]. Also, assumptions must be made in specifying the temperature profile (for matching the brightness temperature to an altitude) in convective overshoots that are necessarily mixing with the ambient environment (see section 2.1).

The approach used here does not include mixing along the trajectory paths. Each parcel is treated independently, and mixing is effectively treated by averaging the final concentrations from multiple trajectories ending in a latitude/longitude grid box. Isentropic exchange between the TTL and the extratropical lower stratosphere can be a significant term in the budget of TTL tracers, particularly during Boreal summertime and for species with strong concentration contrasts between the two regions [*Konopka et al.*, 2010]. *Ploeger et al.* [2012] showed that isentropic mixing into the TTL is important for ozone, which has a strong meridional gradient but relatively weak for CO, which has little TTL-extratropical-stratosphere gradient. Our trajectory approach should include in-mixing from the extratropics to the extent that the MERRA wind fields properly represent the latitudinal dispersion of trajectories; however, our approach does not include small-scale mixing effects.

6. Results

We begin by showing results from a Boreal wintertime set of 45 day trajectories ending 1–7 February 2007 and a summertime set of trajectories ending 25–31 August 2007. For each time period, we have run one set of simulations with convective influence included and another set with convective influence excluded. In addition, we use sensitivity tests to evaluate the impacts of factors such as the convective cloud-top height, α_{conv}, the distribution of TTL radiative heating, and the distribution of CO loss rates (essentially corresponding to variations in OH concentration). The sensitivity to the length of the trajectories is evaluated, and calculations for additional weeks are used to show that the results are not unique to the

Table 1. List of 100 hPa CO Simulation Sets

Simulation	Correlation	RMS Error	Offset[a]	Rel. RMS Error[b]
1–7 Feb baseline[c]	0.72	9.3	−3.5	8.6
1–7 Feb no convection	0.67	17.1	−13.5	10.5
1–7 Feb $\alpha_{conv} = 0.5$	0.84	10.0	−7.8	6.3
1–7 Feb $\theta_{conv} - 3$ K	0.86	10.3	−8.3	6.1
1–7 Feb zonal mean heating	0.64	11.6	−6.4	9.7
1–7 Feb zonal initial CO	0.72	9.5	−3.7	8.7
1–7 Feb no conv., zonal mean heating	0.40	27.1	−24.9	10.7
1–7 Feb heating rate +0.15 K d^{-1}	0.79	9.0	3.8	8.2
1–7 Feb heating rate −0.15 K d^{-1}	0.79	13.4	−11.2	7.4
1–7 Feb column mean WACCM conv. CO	0.75	10.7	−7.3	7.7
1–7 Feb zonal mean CO loss rate	0.72	18.5	−16.0	9.3
1–7 Feb 60 day trajectories	0.73	9.5	−3.9	8.6
25–31 Jan $\alpha_{conv} = 1$	0.71	13.0	5.0	12.0
25–31 Jan $\alpha_{conv} = 0.5$	0.70	9.3	−0.2	9.3
8–14 Feb $\alpha_{conv} = 1$	0.78	9.2	4.5	8.0
8–14 Feb $\alpha_{conv} = 0.5$	0.79	6.5	−0.1	6.5
25–31 Aug baseline	0.88	8.2	−6.5	4.9
25–31 Aug no convection	0.69	16.6	−15.1	6.8
25–31 Aug $\alpha_{conv} = 0.5$	0.90	8.8	−7.5	4.7
25–31 Aug zonal mean heating	0.88	7.8	3.2	7.1
25–31 Aug zonal initial CO	0.89	6.9	−2.9	6.3
25–31 Aug no conv., zonal mean heating	0.26	15.9	−13.3	8.7
25–31 Aug heating rate +0.1 K d^{-1}	0.89	10.3	5.6	8.5
25–31 Aug heating rate −0.1 K d^{-1}	0.88	11.7	−10.5	5.2
25–31 Aug zonal mean CO loss rate	0.90	17.2	−15.3	7.9
25–31 Aug column mean WACCM CO	0.90	7.2	−10.4	6.1
25–31 Aug 60 day trajectories	0.89	8.1	−6.3	5.0
18–24 Aug $\alpha_{conv} = 1$	0.83	7.4	0.0	7.4
18–24 Aug $\alpha_{conv} = 0.5$	0.88	5.8	0.0	5.8
11–17 Aug $\alpha_{conv} = 1$	0.91	8.5	0.3	8.5
11–17 Aug $\alpha_{conv} = 0.5$	0.92	5.9	−0.3	5.9

[a]Mean difference between model and MLS 100 hPa CO concentrations.
[b]RMS difference after subtraction of mean model versus MLS difference.
[c]Including convection, using boundary-layer WACCM CO for convective influence, $\alpha_{conv} = 1$, 45 day trajectories.

particular periods chosen. The sets of simulations are listed in Table 1 along with statistical measures of the comparisons with the spatial distribution of MLS CO at 100 hPa.

6.1. Boreal Winter

The 1–7 February global distributions of 100 hPa CO is compared with MLS measurements in Figure 8. As discussed above, back trajectories sets were launched every 6 h over the 1 week time periods. For each set of trajectories corresponding to a particular end time, we average the final CO concentrations in 20° longitude by 10° latitude bins such that we have sufficient statistics of CO versus pressure to apply the MLS CO averaging kernels and generate 100 hPa values for comparison with the MLS retrievals. The resulting 100 hPa CO values in the 20° by 10° bins are then averaged over the 1 week periods, resulting in the maps shown in Figures 8. Averaging the MLS values over 1 week periods and in 10° by 20° grid boxes provides at least 62 measurements per grid box, producing a robust measure of the grid-box mean. The correlation coefficients, offsets, and root-mean square errors provided in Table 1 were calculated using the weekly means of the 20° by 10° bins.

During wintertime, the dominant features in the 100 hPa MLS CO distribution are relative enhancements over central Africa and the Americas (presumably associated with convective transport of polluted air) and a broad maximum over the central and western Pacific. The trajectory simulations including convective influence generally reproduce each of these features (Figure 8, bottom), although the CO mixing ratio
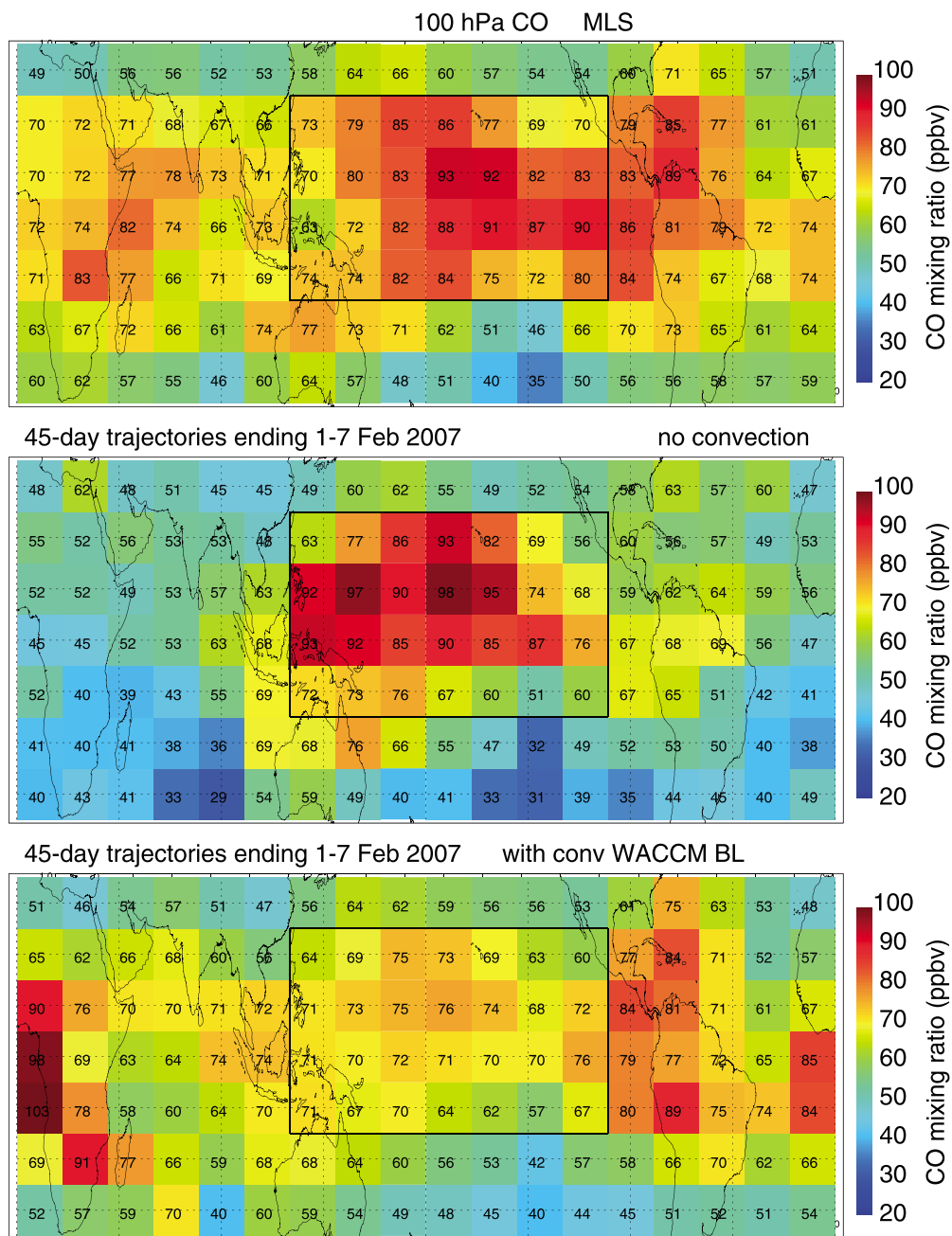
Figure 8. Maps of 1–7 February 2007. 100 hPa CO are shown from (top) MLS measurements, (middle) trajectory simulations excluding convection, and (bottom) trajectory simulations including convective influence. See text for discussion.

over the Pacific is suppressed compared to the MLS measurements, and the direct influence of continental convection over Africa seems to be exaggerated, particularly over western Africa and the neighboring Atlantic region. The excess CO over western Africa is consistent with the excessive African CO emissions in the WACCM simulation (see section 4). The exaggerated convective influence in the model is perhaps not surprising given that we are assuming that air having boundary-layer CO concentrations is transported to the TTL without dilution.

In the set of simulations without convective influence (Figure 8, middle), the African CO maximum is absent (as expected), but the high CO region over the Pacific is actually enhanced. It turns out that over the Pacific, convective transport of relatively clean, lower tropospheric air to the TTL decreases CO at 100 hPa. Closer
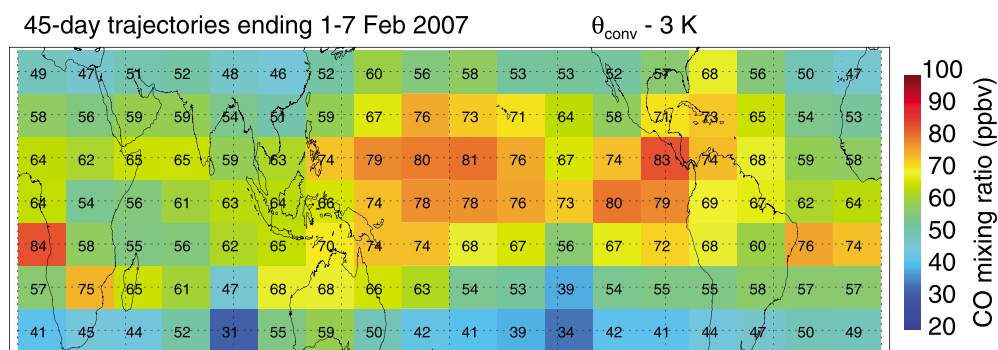
Figure 9. Map of 1–7 February 2007. 100 hPa CO is shown for a set of simulations with the distribution of convective cloud-top potential temperatures shifted down by 3 K.

examination reveals that the strong western/central-Pacific enhancement in 100 hPa CO concentration in the simulations without convective influence is a result of the combination of the negative vertical gradient in TTL CO and the global distribution of TTL radiative heating, which exhibits a strong maximum in the western Pacific associated with the high occurrence frequency of upper tropospheric clouds in the region. In other words, the strong TTL uplift over the Pacific along with the decrease in CO with increasing altitude result in an enhancement of 100 hPa CO concentration. The strong Pacific uplift also reduces the residence of time of parcels in the TTL in this region, thereby limiting the time for photochemical loss of CO, further enhancing the 100 hPa CO concentration in the region. In fact, when we repeat the no-convection set of trajectory simulations with a flat (zonal mean) TTL heating rate field, the Pacific CO maximum is completely absent (not shown).

The distribution of 100 hPa CO indicated by MLS appears to lie somewhere between the simulation results with full convective influence ($\alpha_{conv} = 1$) and the results with no convective influence (Figure 8). As this comparison suggests, using an intermediate value of α_{conv} (such that the CO concentration at the point of convective influence is specified as a mixture of the local concentration and the convective influence value) produces a distribution that correlates better with the MLS distribution (see Table 1). This result is physically reasonable since some mixing between the convective plumes and the environment must be occurring, implying $\alpha_{conv} < 1$.

The relative abundance of 100 hPa CO over the Pacific versus over continental regions is strongly sensitive to the height of convective influence as well. Figure 9 shows the impact of decreasing the cloud-top potential temperatures determined from satellite observations by 3 K (corresponding to about 0.5 km in the upper TTL). Even this relatively small decrease in convection height significantly suppress the 100 hPa CO mixing ratio over continental convective regions (particularly western Africa) and enhances the CO maximum over the Pacific. The result is an improvement in the spatial correlation with MLS CO observations ($r = 0.86$ in the $\theta_{conv} - 3$ K set of simulations versus $r = 0.72$ for the baseline set). This 3 K offset is similar to the uncertainty in cloud-top heights derived from infrared satellite techniques.

Focusing on the region of relatively high CO mixing ratios over the Pacific, we next examine the trajectories ending at pressures near 100 hPa (between 75 and 125 hPa) to identify the most important CO convective sources contributing to this ensemble. Figure 10 shows the geographic distribution of these convective sources, with color coding indicating the height (potential temperature) of the convective encounters. Over 50% of the 100 hPa CO in the Pacific region comes from the western Pacific convection, with a significant contribution from convection over the maritime continent (17%) where convection extends to particularly high potential temperatures, and minor contributions from Australia (1.3%), Africa (5%), and South America (1.2%). Trajectories that did not intersect convection account for 16% of the CO in the Pacific region near 100 hPa.

6.2. Boreal Summer

During summertime, the Asian monsoon and its associated anticyclone dominate the 100 hPa CO distribution. The Asian summer monsoon anticyclone (AAC) CO maximum has been investigated in a number of previous studies [e.g., *Filipiak et al.*, 2005; *Li et al.*, 2005]. In particular, recent studies have investigated transport pathways leading to the observed tracer distribution in the AAC. *Fu et al.* [2006] argued based
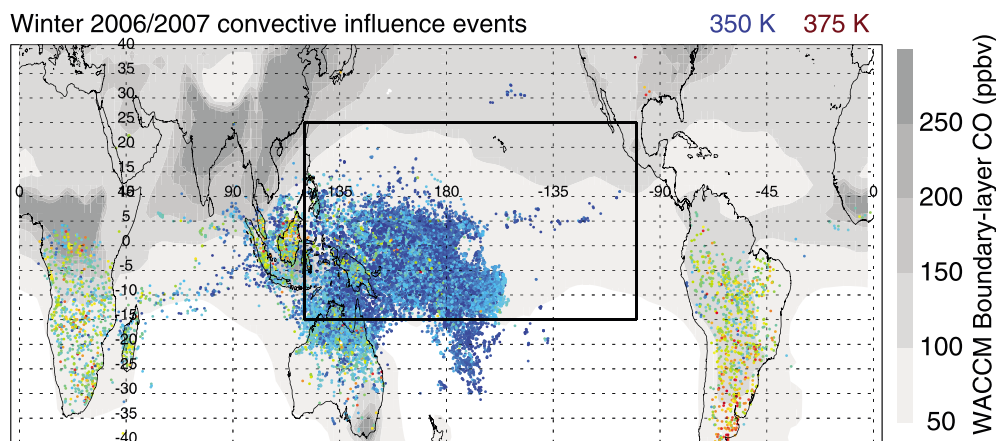
Figure 10. The colored dots indicate the locations of convective encounters for parcels ending inside the black box over the Pacific and at pressures within 25% of 100 hPa. The colors of the dots indicate the potential temperatures of the convective encounters, with blues in the lower TTL (near 350 K potential temperature) and reds near the tropopause (375 K). The gray shading indicates the WACCM boundary-layer CO concentration.

on satellite measurements of tracers and convection that convection over the Tibetan Plateau dominates cross-tropopause transport in the AAC region. *Park et al.* [2007] analyzed large-scale meteorological model fields along with satellite observations of tracers, and they concluded that upward transport on the eastern end of the anticyclone may be important for transporting tracers from the mean convective-detrainment level near 12 km up to the tropopause level. *Park et al.* [2009] used a global chemical transport model to further show that India and Southeast Asia are the dominant source regions for CO that gets transported to the tropopause. *Bergman et al.* [2013] used kinematic trajectory analysis to show that transport to the AAC occurs primarily through a midtroposphere conduit centered near the southern edge of the Tibetan plateau where the region of strong convective vertical motions overlaps with the confined anticyclone region.

The comparison between our trajectory model results and the MLS CO distribution (Figure 11) supports the expectation that that the AAC CO maximum is produced by deep convective transport of polluted air to the TTL. Not surprisingly, the AAC CO feature is essentially absent in the trajectory simulations that omit convective influence. Since we are using the MLS CO measurements to specify the concentration at the earliest trajectory times, the initial CO field includes a distinct AAC enhancement even in the simulations without convective influence. However, the anticyclone is not completely isolated, and the high-CO AAC parcels detrain and are dispersed throughout the tropics within a few weeks. The deep tropics CO concentration in the model with convection is somewhat lower than indicated by MLS observations; however, as shown by [*Park et al.*, 2013], the MLS CO measurement may have a high bias on the order of 10 ppbv.

A basic question about the processes leading to the 100 hPa AAC CO enhancement is the relative importance of two transport pathways [*Park et al.*, 2007]: (1) deep convection transport to the vertical level ($\simeq$12–13 km) where detrainment maximizes, followed by slow ascent to 100 hPa, and (2) direct injection of polluted air near the tropopause by the outlier overshooting convective systems. Following [*Dessler et al.*, 2007], we address this issue by running a sequence of calculations excluding convective influence above successively lower potential temperatures. Figure 12 shows the impact on the late August distribution of CO at 100 hPa. Most of the CO enhancement in the anticyclone over Asia comes from convection above 360 K potential temperature, and convection with tops above 365 K contributes significantly. This result is expected given that the *Yang et al.* [2010] heating rates we are using to diagnose vertical wind speed are (on average) only positive above about 360 K (see Figure 4). Detrainment from convection below this level will generally sink back down into the middle troposphere. (Note that in the Asian monsoon anticyclone region, the tropopause is relatively high and often well above 100 hPa. We are not addressing the question of how often convection directly injects air above the tropopause. Rather, we are investigating the transport pathways affecting 100 hPa CO.)
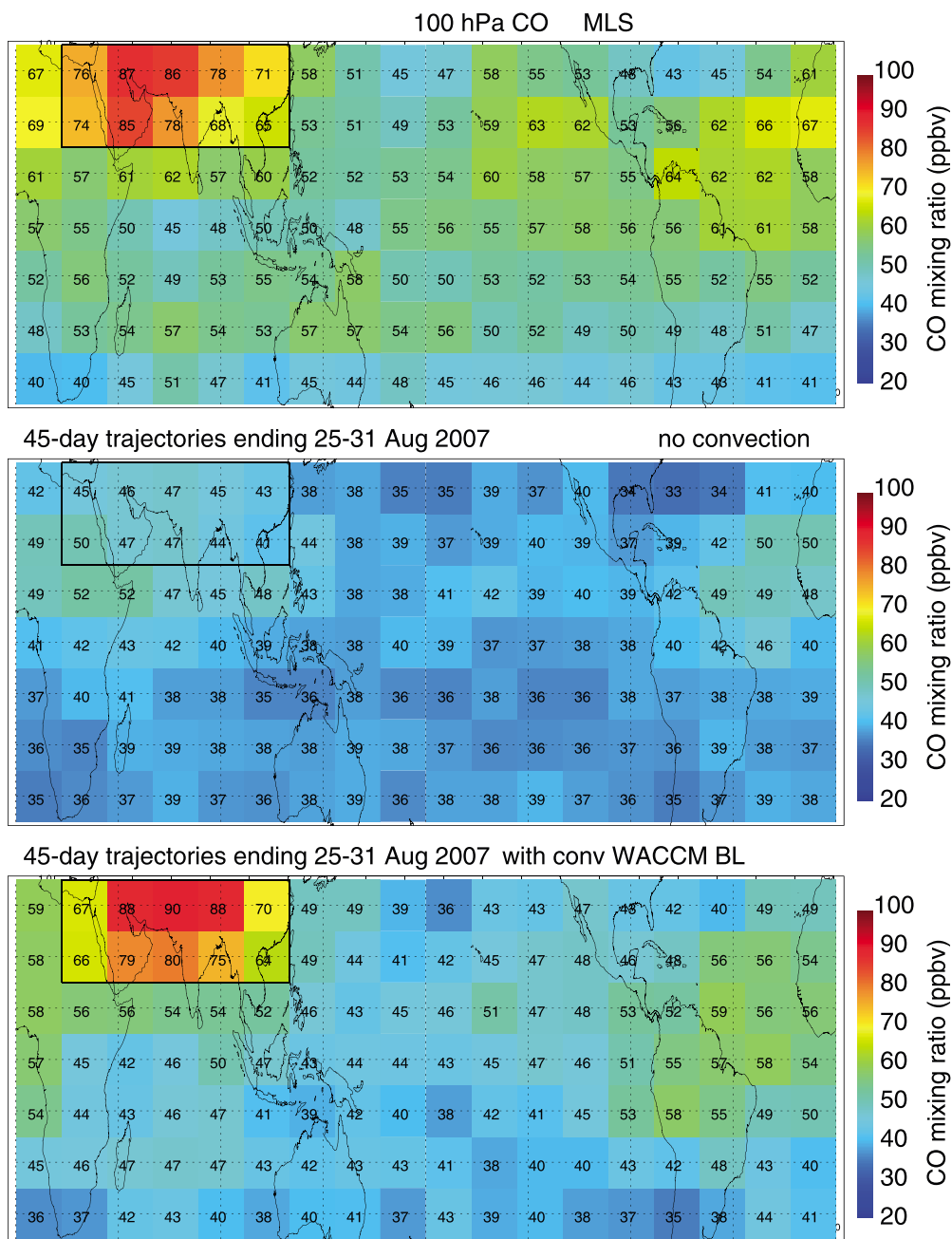
Figure 11. Maps of 25–31 August 2007. 100 hPa CO are shown from (top) MLS measurements, (middle) trajectory simulations excluding convection, and (bottom) trajectory simulations including convective influence. See text for discussion.

The locations of convective influence events contributing to the AAC 100 hPa CO concentration are shown in Figure 13. Continental convection associated with the Asian summertime monsoon dominates, with the highest convection occurring at latitudes north of 20–25°N. Our calculations indicate convection over the Tibetan Plateau contributes significantly (45%) to the AAC 100 hPa CO, with convection over India (32%) accounts for most of the remaining CO. Convection over other regions makes minor contributions: east China (4%), southeast Asia (3%), and the Bay of Bengal (<1%). Similar to the wintertime Pacific calculations, trajectories that did not intersect convection contribute about 15% to the 100 hPa CO.
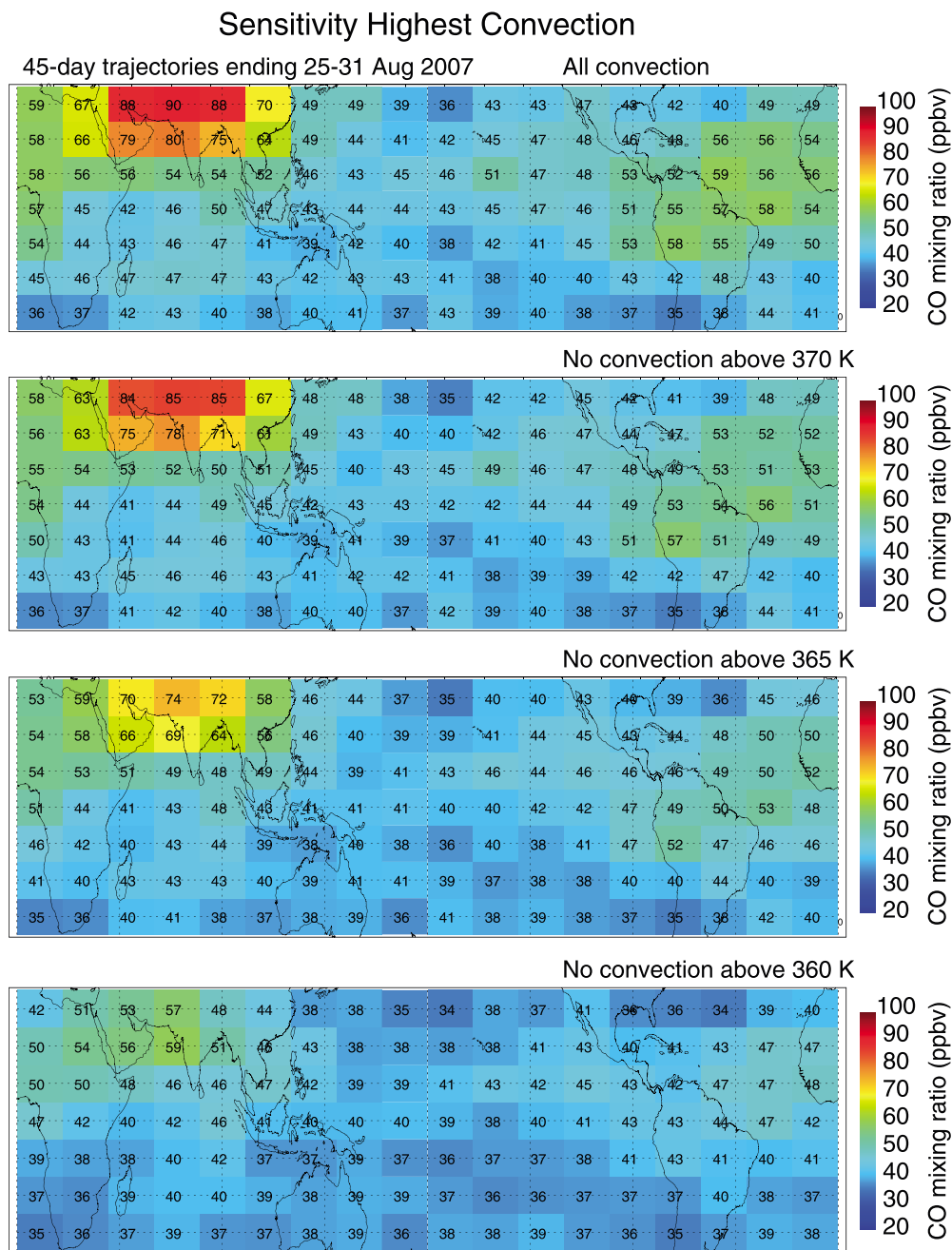
Figure 12. Maps of 25–31 August 2007. 100 hPa CO are shown from trajectory calculations including all convective influence events (top), and from calculations excluding convective influence events above successively lower potential temperatures (370, 365, and 360 K; lower three panels). Much of the AAC CO enhancement comes from the rare convective systems that reach near the tropopause (above ≃365 K potential temperature). The monsoon convection and anticyclone CO enhancement seem to have relatively little affect on the CO concentration elsewhere in the tropics.

6.3. Additional Sensitivities

Here we investigate the sensitivity of the simulated CO fields to MLS distribution of CO used for initializing the trajectories, the distribution, and amplitude of TTL radiative heating, the WACCM distribution of CO loss rate, the WACCM tropospheric CO concentration used for convective influence calculations, and the length of the trajectories. The initialization of parcel CO concentrations using MLS measurements is uncertain both because of the inherent uncertainties in the retrievals and because of the spatial coarseness of the data (both vertically and horizontally). It turns out that using zonal mean MLS CO concentrations for the
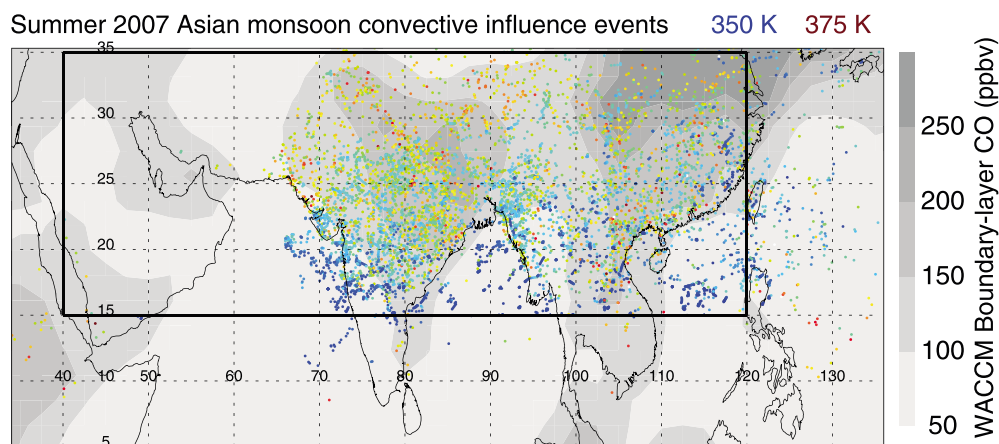
Figure 13. The colored dots indicate the locations of convective encounters for parcels ending inside the black box encompassing the Asian monsoon anticyclone and at pressures within 25% of 100 hPa. The colors of the dots indicate the potential temperatures of the convective encounters, with blues in the lower TTL (near 350 K potential temperature) and reds near the tropopause (375 K). The gray shading indicates the WACCM boundary-layer CO concentration.

initialization produces results that are nearly identical to the baseline results including geographic CO variations for the initialization (see Table 1). This result is perhaps not surprising since most of the trajectories include convective influence that modifies the parcel CO concentration, thereby limiting dependence on the initial conditions. Also, the vertical gradients in initial distribution of TTL CO appear to have a larger impact on the calculations than the horizontal gradients.

As discussed above, the heating rates calculated by *Yang et al.* [2010] are uncertain primarily because of deficiencies in the satellite retrievals of cloud properties. We have run two types of tests to evaluate the impact of heating rate distributions and magnitudes on our calculations of 100 hPa CO. In one set of simulations, we use the zonal mean (still height-dependent) heating rate to determine the impact of the large degree of heating rate regional variability. In another set of sensitivity tests, we increase or decrease the heating rate by a constant offset of 0.15 K d^{-1}. In the wintertime calculations with zonal mean heating rates, the CO maximum over the Pacific is absent (both with and without convective influence), and the correlation with MLS CO observations is lower than in the baseline simulation. Using the zonal mean heating rate instead of the variable heating rate in the summertime calculations has negligible impact on the results. This lack of sensitivity to heating rate variation may result from the fact that the summertime heating rates are more zonally symmetric (outside the AAC) than are the wintertime heating rates. Both the summertime and wintertime calculations are relatively insensitive to increasing or decreasing the heating rate by 0.15 K d^{-1}. This result is somewhat surprising given that 0.15 K d^{-1} is about equal to the mean heating rate in the summer and a sizeable fraction of the mean heating rate in the winter. Perhaps the lack of sensitivity stems from the steep vertical gradient in heating rate near the zero-radiative heating altitude. This steep gradient implies that adding or subtracting a constant offset to the heating rate has little impact on the potential temperature where heating rate changes sign.

As discussed above, the CO loss rate is calculated by dividing the WACCM CO concentrations by the CO tendencies, and the resulting CO loss rate field has a great deal of regional variability. The CO loss rate is directly proportional to the OH concentration in the model, and as discussed above, simulated OH concentrations are uncertain, with dependencies on a plethora of other species that are oxidized by OH. In addition, there is a general dearth of OH observations for evaluating and/or improving the WACCM OH. Using the zonal mean CO loss rate for the wintertime calculations suppresses the concentration over the Pacific, resulting in a large increase in the offset with MLS measurements. In the summertime calculations, using the zonal mean CO loss rate suppresses the CO concentration everywhere outside the AAC, resulting in degradation of the comparison with MLS.

As discussed above, using trajectories longer than 45 days has little impact on the calculated distribution of 100 hPa CO; the spatial patterns statistical agreement with MLS (Table 1) based on 60 day trajectory

calculations are nearly identical to the 45 day trajectory results. This result is expected partly because most of the trajectories already intersected convection with 45 day trajectories (at least for Boreal wintertime).

Lastly, we have used the trajectory model to calculate 100 hPa concentrations for additional 1 week periods during Boreal wintertime and summertime 2007. The comparisons with MLS (in terms of spatial correlation and offset, Table 1) for these weeks are equivalent to the 1 week periods we focused on above. For all but one of the 1 week periods examined, including some degree of mixing between the convective plumes and the local environment ($\alpha_{conv} = 0.5$) results in improved agreement with MLS.

7. Summary and Discussion

We have used a trajectory model to calculate CO concentration in the tropical tropopause layer. Convective influence is diagnosed by tracing the trajectories through geostationary satellite measurements of convective cloud-top heights, the CO concentration detrained from convection is specified using output from WACCM simulations, and the rate of CO loss by OH oxidation is taken from the WACCM simulations. For comparison with the Microwave Limb Sounder observations, we convolve the calculated vertical distributions of CO with the broad MLS CO averaging kernel. Despite considerable uncertainties associated with entrainment into convective updrafts throughout the lower–middle troposphere and dilution of convective plumes in the TTL, the model reproduces most of the prominent features in the early February MLS 100 hPa tropical distributions of CO (Figure 8), and the model properly simulates the structure and magnitude of the AAC CO maximum during late August (Figure 11).

Simulations with and without convective influence show that transport of air with lower tropospheric CO concentration to the TTL by deep convection has a strong impact on the 100 hPa CO geographic distribution. During Boreal wintertime, the CO enhancements over Africa and the Americas clearly result from deep continental convective transport of polluted air to the TTL. Convection over the Pacific basin appears to suppress 100 hPa CO concentrations in the region by transporting clean maritime airmasses to the TTL. In fact, the MLS-observed enhancement of CO over a broad Pacific region appears to be largely a result of the geographic distribution of TTL radiative heating rate, which has a strong maximum over the Pacific associated with the frequent cloud occurrence in the region (see Figure 3). The regional distribution of CO loss rates also has a significant impact on the wintertime CO distribution.

The calculations presented here suggest that the extreme convective systems extending well above the maximum convective detrainment level and well into the upper TTL (above about 360–365 K potential temperature) are responsible for much of the summertime enhancement in the Asian monsoon anticyclone (Figure 12). The relative importance of the highest convective influence events is a direct result of the TTL heating rates used that are (on average) only positive (upward motion) above about 360–365 K in the summer (Figure 4). We also find that the enhanced CO in the summertime Asian monsoon anticyclone "drains" within a few weeks without the CO source from the monsoon convection.

The model is also used to quantify the relative contribution of various lower tropospheric CO source regions to TTL CO abundance. As mentioned above, the maxima in 100 hPa CO over Africa and the Americas is dominated by transport of enhanced lower tropospheric CO in these continental regions to the TTL. The 100 hPa CO in the broad region of moderate enhancement over the wintertime Pacific has contributions both from Pacific maritime convection as well as convection over the maritime continent.

The predominant convective source regions for the enhanced summertime AAC CO in our calculations are the Tibetan Plateau (45%) and India (32%). Our finding that the Tibetan Plateau convection plays an important role in transport to the TTL AAC is consistent with the past analysis by *Fu et al.* [2006] (based on satellite data) and *Bergman et al.* [2013] (based on kinematic trajectories). Our results contrast with the analysis by *Park et al.* [2009] using a chemical transport model and satellite observations, which suggested a larger contribution to 100 hPa CO from east China and very little contribution from the Tibetan Plateau. It is possible that this discrepancy may be at least partially explained by differences between the distribution of parameterized deep convection in the global-model simulations used by [*Park et al.*, 2009] and the observed distribution of convection.

The distributions of CO calculated with the convectively influenced trajectory approach depend on a number of input and forcing fields, including MLS CO retrievals for CO initialization, MERRA horizontal winds for calculating trajectory paths, diabatic heating rates for diagnosing vertical motion, satellite cloud

products for determining convective influence locations and height distributions, WACCM CO fields for specifying convective detrainment, and WACCM CO tendency fields for specifying CO loss rates. Each of these fields has inherent uncertainties. Sensitivity experiments indicate that the results are weakly dependent on the MLS CO fields used for initialization and moderately sensitive to the WACCM CO concentrations and tendencies used for calculating convective detrainment concentrations and OH-driven loss rates. Calculations for different weeks in the winter and summer of 2007 suggest the results are not unique to the specific weeks chosen; however, our analysis does not preclude strong interannual variability in TTL transport processes.

The relatively strong sensitivity of the tropical tropopause CO concentrations (and perhaps other tracers) to the TTL heating rates implies a need for accurate representation of the heating rates in global chemistry-climate models. The accuracy of calculated TTL radiative heating rates will depend on how well the models represent thermal structure, water vapor, and ozone within the TTL, as well as clouds throughout the troposphere. As noted by above, the heating rate fields in modern reanalyses are quite different from the off-line calculations using global cloud measurements, both in terms of geographic distribution and height distribution. The reanalysis fields in each model differ from the other models as well. Since the modern reanalysis models have quite accurate temperature fields, these heating rate differences are most likely dominated by differences in cloud distributions and cloud properties. From the TTL transport perspective, it would be particularly useful to evaluate and improve the representations of clouds in the uppermost tropical troposphere.

The strong sensitivity of the CO distribution to the vertical distribution of convective detrainment into the TTL suggests another potential transport process that should be evaluated carefully in global models. Evaluation (and possible improvement) of the distribution of deep convection cloud-top heights predicted by global-model convective parameterizations is recommended based on this analysis.

References

Adler, R. F., and R. A. Mack (1986), Thunderstorm cloud top dynamics as inferred from satellite observations and a cloud top parcel model, *J. Atmos. Sci.*, *43*, 1945–1960.

Bannister, R. N., A. Oneill, R. Gregory, and K. M. Nissen (2004), The role of the south-east Asian monsoon and other seasonal features in creating the "tape-recorder" signal in the unified model, *Q. J. R. Meteorol. Soc.*, *130*, 1531–1554.

Bergman, J. W., E. J. Jensen, L. Pfister, and Q. Wang (2012), Seasonal differences of vertical-transport efficiency in the tropical tropopause layer: On the interplay between tropical deep convection, large-scale vertical ascent, and horizontal circulations, *J. Geophys. Res.*, *117*, D05302, doi:10.1029/2011JD016992.

Bergman, J. W., F. Fierli, E. J. Jensen, S. Honomichl, and L. L. Pan (2013), Boundary layer sources for the Asian anticyclone: Regional contributions to a vertical conduit, *J. Geophys. Res. Atmos.*, *118*, 2560–2575, doi:10.1002/jgrd.50142.

Brewer, A. M. (1949), Evidence for a world circulation provided by the measurements of helium and water vapor distribution in the stratosphere, *Q. J. R. Meteorol. Soc.*, *75*, 351–363.

Butchart, N. (2014), The Brewer-Dobson circulation, *Rev. Geophys.*, *52*, 157–184, doi:10.1002/2013RG000448.

Dessler, A. E., T. F. Hanisco, and S. Fueglistaler (2007), Effects of convective ice lofting on H_2O and HDO in the tropical tropopause layer, *J. Geophys. Res.*, *112*, D18309, doi:10.1029/2007JD008609.

Emanuel, K. A. (1987), The dependence of hurricane intensity on climate, *Nature*, *326*, 483–485.

Emmons, L. K., et al. (2010), Description and evaluation of the Model for Ozone and Related chemical Tracers, version 4 (MOZART-4), *Geosci. Model Dev.*, *3*, 43–67.

Filipiak, M. J., R. S. Harwood, J. H. Jiang, Q. Li, N. J. Livesey, G. L. Manney, W. G. Read, M. J. Schwartz, J. W. Waters, and D. L. Wu (2005), Carbon monoxide measured by the EOS Microwave Limb Sounder on Aura: First results, *Geophys. Res. Lett.*, *32*, L14825, doi:10.1029/2005GL022765.

Fu, R., Y. L. Hu, J. S. Wright, J. H. Jiang, R. E. Dickinson, M. X. Chen, M. Filipiak, W. G. Read, J. W. Waters, and D. L. Wu (2006), Short circuit of water vapor and polluted air to the global stratosphere by convective transport over the Tibetan Plateau, *Proc. Natl. Acad. Sci.*, *103*, 5664–5669.

Fueglistaler, S., H. Wernli, and T. Peter (2004), Tropical troposphere-to-stratosphere transport inferred from trajectory calculations, *J. Geophys. Res.*, *109*, D03108, doi:10.1029/2003JD004069.

Fueglistaler, S., A. E. Dessler, T. J. Dunkerton, I. Folkins, Q. Fu, and P. W. Mote (2009), The tropical tropopause layer, *Rev. Geophys.*, *47*, RG1004, doi:10.1029/2008RG00267.

Garcia, R. R., D. Marsh, D. E. Kinnison, B. Boville, and F. Sassi (2007), Simulations of secular trends in the middle atmosphere, *J. Geophys. Res.*, *112*, D09301, doi:10.1029/2006JD007485.

Gettelman, A., W. J. Randel, F. Wu, and S. T. Massie (2002), Transport of water vapor in the tropical tropopause layer, *Geophys. Res. Lett.*, *29*(1), 1009, doi:10.1029/2001GL013818.

Holton, J., P. H. Haynes, M. E. McIntyre, A. R. Douglass, R. B. Rood, and L. Pfister (1995), Stratosphere-troposphere exchange, *Rev. Geophys.*, *33*, 403–439.

Huffman, G. J., R. F. Adler, D. T. Bolvin, G. Gu, E. J. Nelkin, K. P. Bowman, Y. Hong, E. F. Stocker, and D. B. Wolff (2007), The TRMM multi-satellite precipitation analysis: Quasi-global, multi-year, combined-sensor precipitation estimates at fine scale, *J. Hydrometeorol.*, *8*, 38–55.

Kinnison, D. E., et al. (2007), Sensitivity of chemical tracers to meteorological parameters in the MOZART-3 chemical transport model, *J. Geophys. Res.*, *112*, D20302, doi:10.1029/2006JD007879.

Knutson, T. R., et al. (2010), Tropical cyclones and climate change, *Nat. Geosci.*, *3*, 157–163.

Konopka, P., J.-U. Gross, G. Günther, F. Ploeger, R. Pommrich, R. Müller, and N. Livesey (2010), Annual cycle of ozone at and above the tropical tropopause: Observations versus simulations with the Chemical Lagrangian Model of the Stratosphere (CLaMS), *Atmos. Chem. Phys.*, *10*, 121–132.

Kunz, A., L. L. Pan, P. Konopka, D. E. Kinnison, and S. Tilmes (2011), Chemical and dynamical discontinuity at the extratropical tropopause based on START08 and WACCM analysis, *J. Geophys. Res.*, *116*, D24302, doi:10.1029/2011JD016686.

Lamarque, J.-F., et al. (2012), CAM-chem: Description and evaluation of interactive atmospheric chemistry in the Community Earth System Model, *Geosci. Model Dev.*, *5*, 369–411.

Li, Q., et al. (2005), Convective outflow of South Asian pollution: A global CTM simulation compared with EOS MLS observations, *Geophys. Res. Lett.*, *32*, L14826, doi:10.1029/2005GL022762.

Lin, S.-J. (2004), A "vertically-Lagrangian" finite-volume dynamical core for global atmospheric models, *Mon. Weather Rev.*, *132*, 2293–2307.

Liu, C., E. J. Zipser, and S. W. Nesbitt (2007), Global distribution of tropical deep convection: Different perspectives from TRMM, infrared, and radar data, *J. Clim.*, *20*, 489–503.

Livesey, N. J., et al. (2008), Validation of Aura Microwave Limb Sounder O_3 and CO observations in the upper troposphere and lower stratosphere, *J. Geophys. Res.*, *113*, D15S02, doi:10.1029/2007JD008805.

Marsh, D., M. J. Mills, D. E. Kinnison, R. R. Garcia, J.-F. Lamarque, and N. Calvo (2013), Climate change from 1850–2005 simulated in CESM1 (WACCM), *J. Clim.*, *26*, 7372–7391.

Minnis, P., C. R. Yost, S. Sun-Mack, and Y. Chen (2008), Estimating the top altitude of optically thick ice clouds from thermal infrared satellite observations using CALIPSO data, *Geophys. Res. Lett.*, *35*, L12801, doi:10.1029/2009GL033947.

Mote, P. W., et al. (1996), An atmospheric tape recorder: The imprint of tropical tropopause temperatures on stratospheric water vapor, *J. Geophys. Res.*, *101*, 3989–4006.

Neale, R. B., J. Richter, S. Park, P. H. Lauritzen, S. J. Vavrus, P. J. Rasch, and M. Zhang (2013), The mean climate of the Community Atmosphere Model (CAM4) in forced SST and fully coupled experiments, *J. Clim.*, *26*, 5150–5168.

Park, M., W. J. Randel, L. K. Emmons, and N. Livesey (2009), Transport pathways of carbon monoxide in the asian summer monsoon diagnosed from Model of Ozone and Related Tracers (MOZART), *J. Geophys. Res.*, *114*, D08303, doi:10.1029/2008JD10621.

Park, M., W. J. Randel, D. E. Kinnison, L. K. Emmons, P. F. Bernath, K. A. Walker, C. D. Boone, and N. J. Livesey (2013), Hydrocarbons in the upper troposphere and lower stratosphere observed from ACE-FTS and comparisons with WACCM, *J. Geophys. Res. Atmos.*, *118*, 1964–1980, doi:10.1029/2012JD018327.

Park, S., et al. (2007), The CO_2 tracer clock for the tropical tropopause layer, *Atmos. Chem. Phys.*, *7*, 3989–4000.

Ploeger, F., et al. (2012), Horizontal transport affecting trace gas seasonality in the Tropical Tropopause Layer (TTL), *J. Geophys. Res.*, *117*, D09303, doi:10.1029/2011JD017267.

Randel, W. J., and E. J. Jensen (2013), Physical processes in the tropical tropopause layer and their roles in a changing climate, *Nat. Geosci.*, *6*, 169–176.

Randel, W. J., and M. Park (2006), Deep convective influence on the asian summer monsoon anticyclone and associated tracer variability observed with Atmospheric Infrared Sounder (AIRS), *J. Geophys. Res.*, *111*, D12314, doi:10.1029/2005JD006490.

Randel, W. J., M. Park, L. Emmons, D. Kinnison, P. Bernath, K. A. Walker, and C. Boone (2010), Transport from the Asian monsoon to the stratosphere observed in satellite measurements of hydrogen cyanide, *Science*, *328*, 611–613.

Reinecker, M. M., et al. (2011), MERRA: NASA's modern-era retrospective analysis for research and applications, *J. Clim.*, *24*, 3624–3648, doi:10.1175/JCLI–D–11–00015.1.

Rosenlof, K. H. (1995), Seasonal cycle of the residual mean meridional circulation in the stratosphere, *J. Geophys. Res.*, *100*, 5173–5191.

Schoeberl, M., and A. E. Dessler (2011), Dehydration of the stratosphere, *Atmos. Chem. Phys.*, *11*, 8433–8446.

Schoeberl, M. R., B. N. Duncan, A. R. Douglass, J. Waters, N. Livesey, W. Read, and M. Filipiak (2006), The carbon monoxide tape recorder, *Geophys. Res. Lett.*, *33*, L12811, doi:10.1029/2006GL026178.

Schoeberl, M. R., A. R. Douglass, R. S. Stolarski, S. Pawson, S. E. Strahan, and W. Read (2008), Comparison of lower stratospheric tropical mean vertical velocities, *J. Geophys. Res.*, *113*, D24109, doi:10.1029/2008JD010221.

Sherwood, S. C., J.-H. Chae, P. Minnis, and M. McGill (2004), Underestimation of deep convective cloud tops by thermal imagery, *Geophys. Res. Lett.*, *31*, L11102, doi:10.1029/2004GL019699.

van der Werf, G. R., J. T. Randerson, L. Giglio, G. J. Collatz, P. S. Kasibhatla, and A. F. Arellano Jr. (2006), Interannual variability in global biomass burning emissions from 1997 to 2004, *Atmos. Chem. Phys.*, *6*, 3423–3441.

Wang, T., W. J. Randel, A. E. Dessler, M. R. Schoeberl, and D. E. Kinnison (2014), Trajectory model simulations of ozone (O_3) and carbon monoxide (CO) in the lower stratosphere, *Atmos. Chem. Phys.*, *14*, 7135–7147.

Wang, Z., and K. Sassen (2001), Cloud type and macrophysical property retrieval using multiple remote sensors, *J. Appl. Meteorol.*, *40*, 1665–1682.

Wright, J. S., and S. Fueglistaler (2013), Large differences in the diabatic heat budget of the tropical UTLS in reanalyses, *Atmos. Chem. Phys. Discuss.*, *13*, 8805–8830.

Xiao, Y., D. J. Jacob, and S. Turquety (2007), Atmospheric acetylene and its relationship with CO as an indicator of air mass age, *J. Geophys. Res.*, *112*, D12305, doi:10.1029/2006JD008268.

Yang, Q., Q. Fu, and Y. Hu (2010), Radiative impacts of clouds in the tropical tropopause layer, *J. Geophys. Res.*, *115*, D00H12, doi:10.1029/2009JD012393.